MDPI

Article

LLCZN/PEO/LiPF$_6$ Composite Solid-State Electrolyte for Safe Energy Storage Application

Samuel Adjepong Danquah [1,*] , **Jacob Strimaitis** [1,*], **Clifford F. Denize** [1,*], **Sangram K. Pradhan** [1,*] **and Messaoud Bahoura** [1,2]

1   Center for Materials Research, Norfolk State University, Norfolk, VA 23504, USA; mbahoura@nsu.edu
2   Engineering Department, Norfolk State University, Norfolk, VA 23504, USA
*   Correspondence: s.a.danquah@spartans.nsu.edu (S.A.D.); j.strimaitis@spartans.nsu.edu (J.S.);
     c.f.denize@spartans.nsu.edu (C.F.D.); skpradhan@nsu.edu (S.K.P.)

Abstract: All-solid-state batteries (ASSBs) are gaining traction in the arena of energy storage due to their promising results in producing high energy density and long cycle life coupled with their capability of being safe. The key challenges facing ASSBs are low conductivity and slow charge transfer kinetics at the interface between the electrode and the solid electrolyte. Garnet solid-state electrolyte has shown promising results in improving the ion conductivity but still suffers from poor capacity retention and rate performance due to the interfacial resistance between the electrodes. To improve the interfacial resistance, we prepared a composite consisting of Li$_7$La$_{2.75}$Ca$_{0.25}$Zr$_{1.75}$Nb$_{0.25}$O$_{12}$ (LLCZN) garnet material as the ceramic, polyethylene oxide (PEO) as the polymer, and lithium hexafluorophosphate (LiPF$_6$) as the salt. These compounds are mixed in a stoichiometric ratio and developed into a very thin disc-shaped solid electrolyte. The LLCZN provides a lithium-ion transport path to enhance the lithium-ion conduction during charging and discharging cycles, while the LiPF$_6$ contributes more lithium ions via the transport path. The PEO matrix in the composite material aids in bonding the compounds together and creating a large contact area, thereby reducing the issue of large interfacial resistance. FESEM images show the porous nature of the electrolyte which promotes the movement of lithium ions through the electrolyte. The fabricated LLCZN/PEO/LiPF$_6$ solid-state electrolyte shows outstanding electrochemical stability that remains at 130 mAh g^{-1} up to 150 charging and discharging cycles at 0.05 mA cm^{-2} current. All the specific capacities were calculated based on the mass of the cathode material (LiCoO$_2$). In addition, the coin cell retains 85% discharge capacity up to 150 cycles with a Coulombic efficiency of approximately 98% and energy efficiency of 90% during the entire cycling process.

Keywords: all-solid-state batteries; garnet solid-state electrolyte; lithium-ion transport; electrochemical stability

1. Introduction

All-solid-state batteries (ASSBs) are positioned to lead the battery industry as they seek to overcome the enormous drawbacks of conventional lithium-ion batteries (CLIB), which include leakage, flammability, and environmental toxicity [1–3]. The predominant issue in CLIBs is the selection of a more versatile electrolyte that can operate under any extreme condition without compromising the performance and retention capability of the cell. Most of the liquid electrolytes are composed of lithium hexafluorophosphate (LiPF$_6$) salt dissolved in organic solvents, such as ethylene carbonate (EC), propylene carbonate (PC), dimethyl carbonate (DMC), and their mixtures. Unfortunately, the organic-solvent-based system is extremely flammable, especially in overstressed conditions such as overcharging, short-circuiting, extrusion, and elevated temperatures [4]. These drawbacks limit the use of CLIBs in the automobile and aviation industries, where high energy density and, most importantly, safety are required [1,4–7].

Substituting liquid electrolytes with solid electrolytes is gaining ground as a viable solution for the previously mentioned issues. For example, ASSBs possess increased mechanical strength and thermal tolerance over their CLIB counterparts [1]. A solid-state electrolyte (SSE) also greatly simplifies the architecture of the battery, since the SSE doubles as both an electrolyte and a separator. However, SSEs still need to satisfy the four central electrochemical performance characteristics for electrolytes, which are conductivity, potential window, interfacial kinetics, and transference number [8,9]. In general, SSEs should have: (i) a lithium-ion conductivity greater than 10^{-4} S cm^{-1} at 20 °C, (ii) mechanical stability and toughness to permit the creation of large-area and thin layers that do not break during device assembly or in situ charge–discharge cycling, and (iii) a strong adhesion and large contact area to a lithium anode to allow a low-impedance plating/stripping of Li across the anode/electrolyte interface over long cycle life. In addition, strong bonding of Li to SSE tolerates pulverization of cathode on charge/discharge cycling [9,10]. To this end, a variety of solid-state electrolytes have been proffered, each with unique properties [11]. These can be classified into two categories: organic and inorganic.

Organic SSEs, also known as solid polymer electrolytes (SPEs), such as polyethylene oxide (PEO), and other polycarbonate-based SSEs, such as PEC (polyethylene carbonates), PPC (polypropylene carbonates), and PTMC (polytrimethyl carbonates), exhibit good flexibility, good stability with lithium metal, and easy large-area membrane fabrication [12,13]. In particular, PEO, the most widely investigated Li-ion conducting polymer due to its flexibility and strong binding characteristics, has a high transference number, averaging one Li$^+$ per every four ethylene oxide sites [14]. However, solid polymer electrolytes suffer from low ionic conductivity, low mechanical strength, a limited electrochemical window, and cannot withstand lithium dendrite formation [15–20].

On the other hand, the classic inorganic solid electrolytes, made out of materials such as oxides (e.g., perovskites, garnets), sulfides, hydrides, halides, borates or phosphates and thin-film lithium phosphorus oxynitrides (LIPON), possess high ion conductivity at room temperature in the range of 10^{-7} to 10^{-3} S cm^{-1} [8]. In addition, inorganic solid electrolytes are mechanically stable and show superior Li$^+$ transference numbers [1,11,21,22]. Yet, inorganic solid electrolytes encounter problems in terms of their optimum performance due to their hardness, brittleness, large grain boundary resistance, poor interfacial resistance, and relatively difficult fabrication process. To overcome these drawbacks, myriad additional inorganic materials, such as NASICON (sodium superionic conductor and Li-ion conducting sodium superionic conductor), perovskite-type, garnet-type, lithium superionic conductor (LISICON), sulfides and hybrid solutions are being investigated [1,10,12,23,24]. Unfortunately, despite these advantages, poor wetting properties of garnet SSE and molten Li metal create microscopic gaps at the interface. As a result, it generates large interfacial resistance between the garnet electrolyte and electrode material due to its rigid ceramic nature [25]. To address the issue of large interfacial resistance, other researchers proposed an all-solid-state electrolyte using Li$_5$La$_3$Ta$_2$O$_{12}$ (LLTa) and Li$_7$La$_3$Zr$_2$O$_{12}$ (LLZ) due to their stable nature against lithium metal and their high ion conductivity. Their findings showed a high total conductivity of 3×10^{-4} S cm^{-1} at 25 °C which is better than the other families of solid-state electrolytes mentioned earlier. Furthermore, the study also suggested that zirconium containing lithium garnet is an encouraging solid ceramic electrolyte for all-solid-state lithium-ion rechargeable batteries. The rigid framework of elements such as oxygen, zirconium and lanthanum in the garnet structure results in negligible mobility at operating temperatures and, therefore, the ionic motion is due to the transport of lithium ions [26–28].

Composite solid electrolytes that combine the advantages of both their organic and inorganic components have shown favorable outcomes [29–35]. One type of composite, known as a ceramic/polymer solid electrolyte (CPSE), specifically, shows promise. Chen et al. synthesized CPSE where the ceramic component is the garnet LLZTO, the polymer part is PEO, and salt is lithium bis(trifluoromethanesulfonyl)imide (LiTFSI). Their battery demonstrated a discharge capacity of 127 mAh g^{-1} during the first 50 cycles, with

an ideal Coulombic efficiency of 100%, showing good and stable electrode/electrolyte interfaces during the cycling [14]. In addition, Appetecchi et al. used PEO-LiCF$_3$SO$_3$-based CPSE materials and observed that the conductivity of a host polymer and its interfacial behavior in contact with lithium metal can be improved by the addition of ceramic fillers [34]. The PEO-LiPF$_6$ system reported by Magistris et al. showed a significant higher ionic conductivity of 10^{-4} S cm^{-1} at temperature above the melting point of PEO at ~60 °C. However, the LiPF$_6$ underwent thermal decomposition and reduced to LiF, which evolves gaseous by-products at a temperatures beyond 100 °C. The PEO-LiPF$_6$ system did not work at room temperature, but worked at elevated temperatures [36]. The PEO-LiTFSI-LLZTO (PLL) composite electrolyte with 40% LLZTO content reported by Zhao et al. had an ionic conductivity of 1.2×10^{-5} S cm^{-1} at room temperature with the application of liquid electrolyte. The PLL ionic conductivity increased with increasing testing temperatures. The PLL composite electrolyte impedes dendrites in Li metal anodes because of the addition of LLZTO particles and the reduction in the crystallization of PEO [37]. Although massive progress has been accomplished as a result of these undertakings, more successful techniques are still urgently needed to further improve the performance of the CPSEs.

Hence, we investigate a novel CPSE consisting of Li$_7$La$_{2.75}$Ca$_{0.25}$Zr$_{1.75}$Nb$_{0.25}$O$_{12}$ (LLCZN) garnet material as the inorganic ceramic, PEO as the organic polymer, and lithium hexafluorophosphate (LiPF$_6$) as the ionic salt. This LLCZN/PEO/LiPF$_6$ CPSE is synthesized via a facile sol–gel and pelletizing technique, and then characterized and evaluated by X-ray diffraction (XRD) (Rigaku, Wilmington, DE, USA), field emission scanning electron microscopy (FESEM) (Hitachi, Santa Clara, CA, USA), Fourier-transform infrared spectroscopy (FTIR) (Perkin Elmer, Bridgeport, CT, USA), thermogravimetric analysis (TGA) (Shimadzu scientific instrument, Columbia, NY, USA). Brunauer–Emmett–Teller (BET) analysis (Quantachrome, Ashland, KY, USA), and galvanostatic electrochemical testing (MTI Corporation, Richmond, VA, USA) for its suitability in all-solid-state lithium-ion batteries.

2. Experimental Section

2.1. Materials Preparation

The schematic of the sol–gel synthesis method for LLCZN powder is shown in Figure 1. Stoichiometric quantities of LiNO$_3$ (99.99%, Sigma Aldrich, St. Louis, MI, USA), La(NO$_3$)$_3$•6H$_2$O (99.9%, Sigma Aldrich, St. Louis, MI, USA) Ca(NO$_3$)$_2$•4H$_2$O (99.9%, Sigma Aldrich, St. Louis, MI, USA), ZrO(NO$_3$)$_2$•6H$_2$O (99.9%, Sigma Aldrich, St. Louis, MI, USA) and NbCl$_5$ (99.9%, Sigma Aldrich, St. Louis, MI, USA) were dissolved in deionized water with 10% more addition of the LiNO$_3$ to recoup the evaporated Li during exposure to high temperatures. Additionally, ethylene glycol (Sigma Aldrich, St. Louis, MI, USA) and citric acid (Sigma Aldrich, St. Louis, MI, USA) in a mole ratio of 1:1 are added to the solution. Thereafter, the solution was heated on a hot plate at a temperature of 120 °C for 12 h to obtain a gel-like precursor. This material was dried at 400 °C for 10 h and further calcined at 800 °C for another 10 h to produce the LLCZN powder. Finally, the calcined LLZCN powder was sintered at 1050 °C for 12 h and grounded in a clean mortar and pestle to obtain a smooth LLCZN powder as prepared in a similar fashion as in previous reports [38–40].

PEO with a molecular weight of 1,000,000 g mol^{-1} was dried in a vacuum oven (MTI Corporation, Richmond, VA, USA) for 24 h at a temperature of 50 °C, while the LiPF$_6$ salt was dried in a vacuum oven at 80 °C for 12 h. The sintered LLCZN, dried PEO, and dried LiPF$_6$ powders were kept in an argon-filled environment at <0.5 ppm H$_2$O and O$_2$ levels to prevent exposure to oxygen and water in the atmosphere. The 1:1:1 mass ratio of LLCZN/PEO/LiPF$_6$ was weighed and mixed in an opaque plastic vial and placed on a roller for thorough mixing for 24 h. This mixed powder was pelletized using a hydraulic press with an applied force of 22,000 pounds to obtain a flat disc of solid-state electrolyte. The thickness of the as-prepared composite solid-state electrolyte disc was approximately 250 μm. Subsequently, electron beam evaporation technique was used to grow a 7 nm thin

amorphous layer of SiO_2 on the pellet at the anode side at a growth rate of 0.24 Å s^{-1} with a current of 4 mA and a voltage of 10 kV. This will help to reduce the interfacial between the electrode and the solid polymer electrolyte [41].
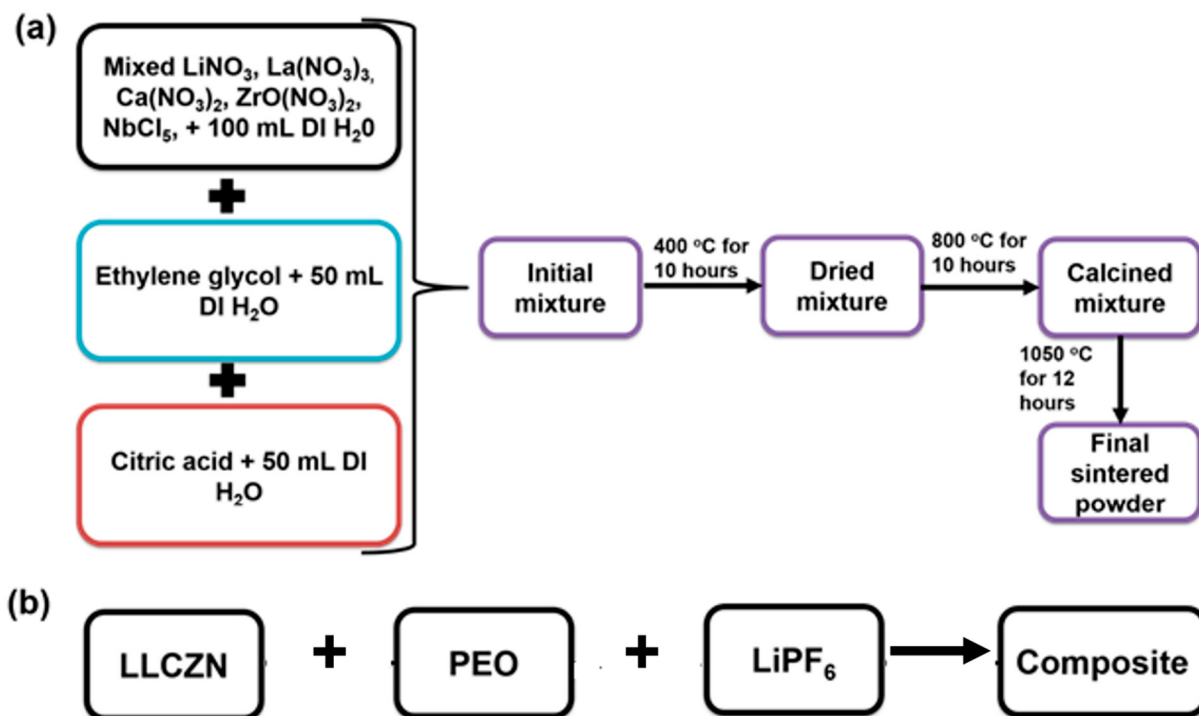

Figure 1. Schematic representation for the synthesis of (**a**) LLCZN powder via sol–gel method and (**b**) composite LLCZN/PEO/LiPF$_6$ in a ratio of 1:1:1 by weight.

2.2. Sample Characterization

To observe the crystal structure of the synthesized LLCZN and the composite LLCZN/PEO/LiPF$_6$ powder, X-ray diffraction was performed with Cu K-alpha radiation at 40 kV and 40 mA over the 2-theta range of 10° to 70°. The surface morphology of the synthesized LLCZN and the composite LLCZN/PEO/LiPF$_6$ solid-state electrolyte was characterized by FESEM. The identification of the functional groups and molecular structures of materials, which in this case includes the organic and polymeric motifs in the solid-state electrolyte and its components were obtained using FTIR in the range of 500 cm^{-1} to 4000 cm^{-1}.

Thermogravimetric analysis (TGA) was performed to assess the thermal stability of the LLCZN/PEO/LiPF$_6$ powder prior to Brunauer–Emmett–Teller (BET) surface analysis to determine the thermal stability of the composite solid-state electrolyte powder. This was also used as a baseline for the degassed temperature in the BET analysis. Approximately 5 mg of the sample was placed in a platinum crucible and then placed into a Shimadzu TGA 50-50H thermogravimetric analyzer. Nitrogen gas with a flowrate of 30 mL was allowed into the pyrolyzing unit to ensure an oxygen-free atmosphere. The sample was heated from room temperature to 600 °C at a heating rate of 10 °C min^{-1} [42].

The Brunauer–Emmett–Teller (BET) surface area, the pore volume, and the pore size of the LLCZN/PEO/LiPF$_6$ solid-state composite are measured using surface area analyzer NOVA 200e. The LLCZN/PEO/LiPF$_6$ solid-state composite powder was degassed at 60 °C as a result of the low melting point of the PEO for 24 h before being adsorbed, and desorbed with N$_2$ at −196 °C. The surface area was evaluated using a multi-point BET model. The pore size distribution was obtained from the desorption isotherm based on the Density-Functional Theory (DFT) model inbuilt software, while the total pore volume is calculated at a relative pressure (p/p$_o$) range of 0.0–1.0. All the models for the BET analysis are built in the NovaWin Software, (Quantachrome, Ashland, KY, USA).

The ionic conductivity of the pristine LLCZN/PEO/LiPF$_6$ disc and the LLCZN/PEO/LiPF$_6$ disc with E-beam ultrathin-layer-coated SiO$_2$ layer at room temperature was measured with CHI660D electrochemical impedance spectroscopy (EIS) (CH Instrument, Shanghai, China) with an applied frequency ranges from high (10^6 Hz) to low (0.01 Hz). The conductivity measurement was performed at a room temperature. The discs were 250 μm thick with an electrode surface area of 0.50 cm^2. The ionic conductivity was calculated using the following formula:

$$\delta = \frac{d}{R_b S}$$

where δ is the ionic conductivity, d is the thickness of the LLCZN/PEO/LiPF$_6$ disc, S is the area of the electrodes contacting with the LLCZN/PEO/LiPF$_6$ composites disc, and R_b is the bulk resistance. The R_b can be derived from the Nyquist impedance plot [43].

2.3. Battery Assembly and Electrochemical Characterization

The ASSB was assembled in a 2032 coin cell, using composite LLCZN/PEO/LiPF$_6$ as an electrolyte, LiCoO$_2$ (LCO) (MTI Corporation, Richmond, VA, USA) as cathodic active material, and Li foil (MTI Corporation, Richmond, VA, USA) as an anode. The cathode slurry was composed of 80 wt.% LCO, 10 wt.% carbon black, and 10 wt.% polyvinylidene fluoride (PVDF) powder (Sigma Aldrich, St. Louis, MI, USA) in N-methyl-2-pyrrolidone (NMP) solvent (Sigma Aldrich, St. Louis, MI, USA). The resulting slurry was coated on a steel plate, partially dried in the open, and kept at 120 °C in a vacuum oven (MTI Corporation, Richmond, VA, USA) for 12 h for further drying. The active material loading on the steel plate was calculated as 5.8 mg cm^{-2}. The ASSB is assembled in an argon-filled glove box (Mbraun Inc., Stratham, NH, USA) with the application of a small amount of lubricating liquid electrolyte (1 M of lithium hexafluorophosphate (LiPF$_6$) in a 1:1 ratio of propylene carbonate (PC) and dimethyl carbonate (DMC), (Sigma Aldrich, St. Louis, MI, USA) between the cathode and the composite LLCZN/PEO/LiPF$_6$ solid-state electrolyte. A BST8-WA (MTI Corporation, Richmond, VA, USA) eight-channel battery analyzer was used to analyze the cycling performance and capacity of the coin cell. The channel of the analyzer had an independent constant-current source in a range of 0.05–1 mA that was programmed and controlled using computer software. Batteries were cycled at room temperature (22–25 °C) with a voltage range of 3 V to 4.5 V at different constant currents.

3. Results and Discussion

The X-ray diffraction graph of the pristine LLCZN powder exhibits a strong peak at 2θ = 30.8° corresponding to the (420) plane, as shown in Figure 2. In addition, the XRD data match the cubic garnet phase of Li$_5$La$_3$Nb$_2$O$_{12}$ (PDF 80-0457), which is the closest crystalline structure reported for LLCZN [40], indicating that our synthesized LLCZN is in a pure cubic phase. The pure cubic phase garnet could lead to a higher lithium-ion conductivity than the tetragonal garnet phase [40]. The XRD data of pristine PEO (Sigma Aldrich, St. Louis, MI, USA) and pristine LiPF$_6$ (Sigma Aldrich, St. Louis, MI, USA) were not examined, because these materials were purchased and not synthesized in our laboratory.
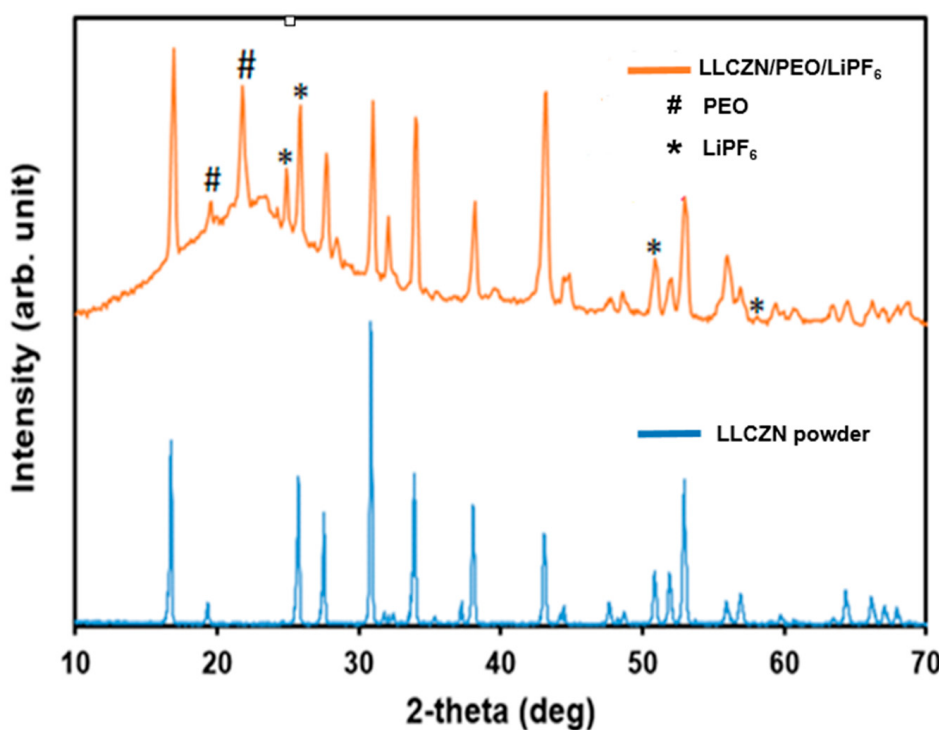
Figure 2. Powder X-ray diffraction patterns of as-prepared LLCZN via sol–gel technique and LLCZN/PEO/LiPF$_6$ composite powder samples.

The XRD results of the composite LLCZN/PEO/LiPF$_6$ powder clearly show similar peaks as the pristine LLCZN. As depicted in Figure 2, the sharp diffraction peaks of the LiPF$_6$ in the composite are observed at 26.8°, which matches the results of Jian-wen Liu et al. [44]. Furthermore, the XRD pattern of the PEO in the composite reveals that the peaks around 19.2° and 23.4° match the XRD peaks described by Ahmed et al. [45] and Bhide et al. [46], signifying the semi-crystalline nature of this polymer. Based on the XRD peaks exhibited in Figure 2, there is an indication that the composite LLCZN/PEO/LiPF$_6$ exhibits the same pure cubic phase as pristine LLCZN by itself. Furthermore, the XRD of the composite material demonstrates that the LLCZN ceramic powder is polycrystalline in nature, without any substantial impurity phases. A change is observed within the XRD pattern of the as-prepared LLCZN/PEO/LiPF$_6$ composite electrolyte as a result of the presence of LiPF$_6$ and PEO. This indicates that the pristine LLCZN garnet, PEO, and LiPF$_6$ are very stable during the preparation process.

The FESEM imaging technique is used to see the surface morphology of the as-prepared composite LLCZN/PEO/LiPF$_6$ powder before pelletizing. The images, shown in Figure 3a–d, indicate that, instead of forming distinctive shapes or arrays, the electrolyte forms an aggregate with particles growing on top of each other or interconnected. The higher magnification images demonstrate that the material is low in density with an abundance of highly interconnected porous structures that favors the lithium-ion intercalation through the electrolyte.
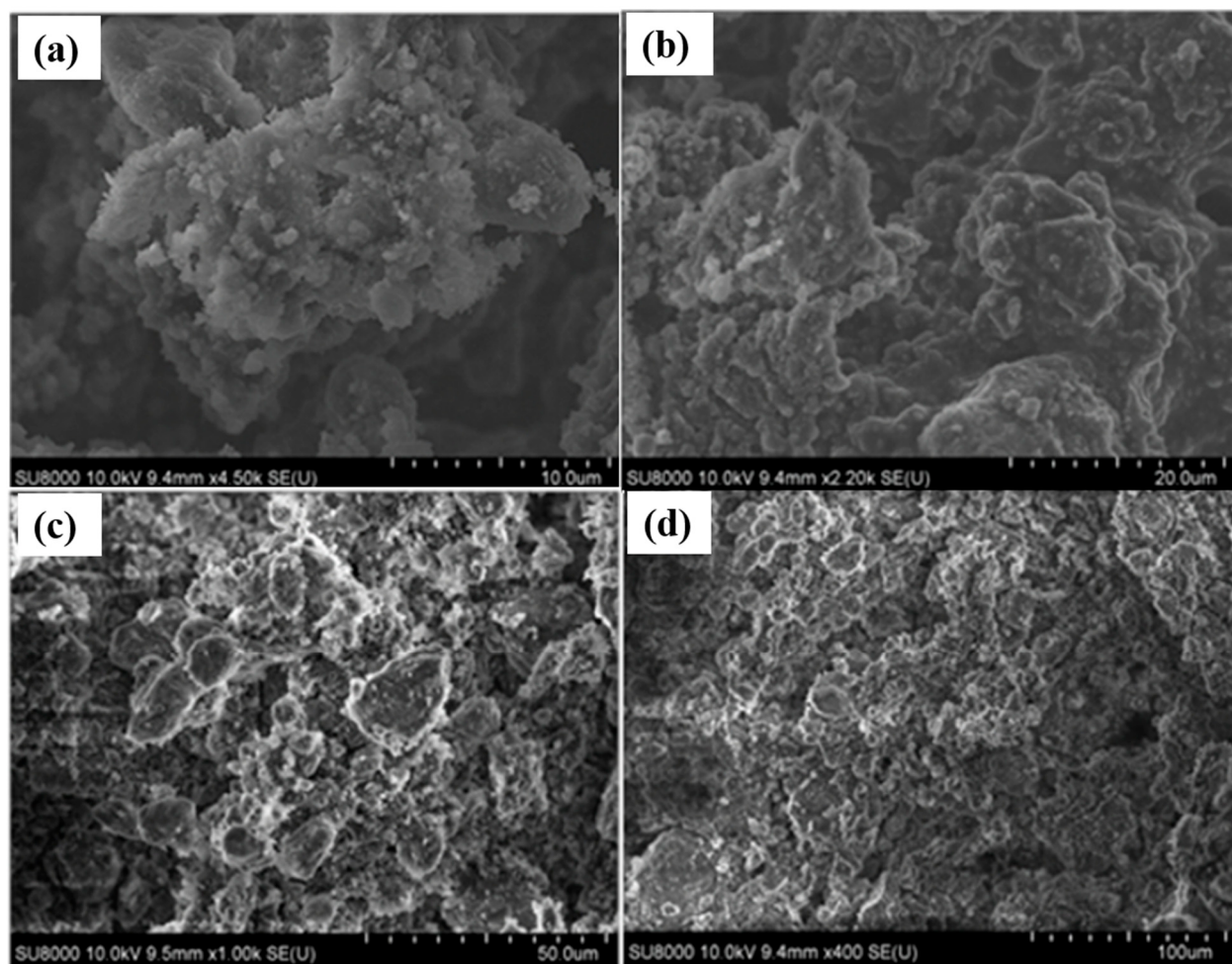
Figure 3. FESEM images of surface morphologies for the composite LLCZN/PEO/LiPF$_6$ powder for solid-state electrolyte before cycling at different magnifications of (**a**) 10.0 μm, (**b**) 20.0 μm, (**c**) 50 μm, and (**d**) 100 μm.

Figure 4 presents the FT-IR spectrum of the individual component materials of the CPSE composite, as well as the IR absorption spectrum of the CPSE. The mid-IR spectrum is divided into four regions as follows: Region A (500 to 1500 cm^{-1}) is the fingerprint, Region B (1500 to 2000 cm^{-1}) is the double bond, Region C (2000 to 2500 cm^{-1}) is the triple bond, and Region D (2500 to 4000 cm^{-1}) is the single bond. The composite material shares several spectral peaks with the component materials, particularly in the "fingerprint region" of the IR spectrum (500–1500 cm^{-1}). A large number of peaks were observed for PEO, LiPF$_6$, and the composite. However, LLCZN, made from different types of higher-mass elements, shows closely spaced frequency vibrations that are typically observed in the fingerprint region. The presence of these bands would be expected to obscure the identification of any of the other components of the composite in this spectral range. However, in the higher frequency range of the spectrum, there are some distinct peaks indicating the presence of each of the individual materials in the composite. Since the relative intensities are a function of both the amount and the absorptivity of the material, the spectra shown in Figure 4 indicate the presence of signature functional groups to confirm the existence of each of the component materials in the composite. The observation of strong peaks at 2890 cm^{-1} and 1280 cm^{-1} in the IR spectrum of the PEO sample is due to the C–H stretching vibration, which is visible in both pristine PEO and in the composite structure. A small but sharp vibration peak at 3750 cm^{-1} corresponding to an O–H vibration along with a pronounced frequency tail appears in both the pristine LLCZN and the composite. The sharp peak at 3607 cm^{-1}, which only appears in LiPF$_6$, can also be seen in the composite material.

Taken together, it can be seen that our prepared composite contains each of the component materials [46–50].
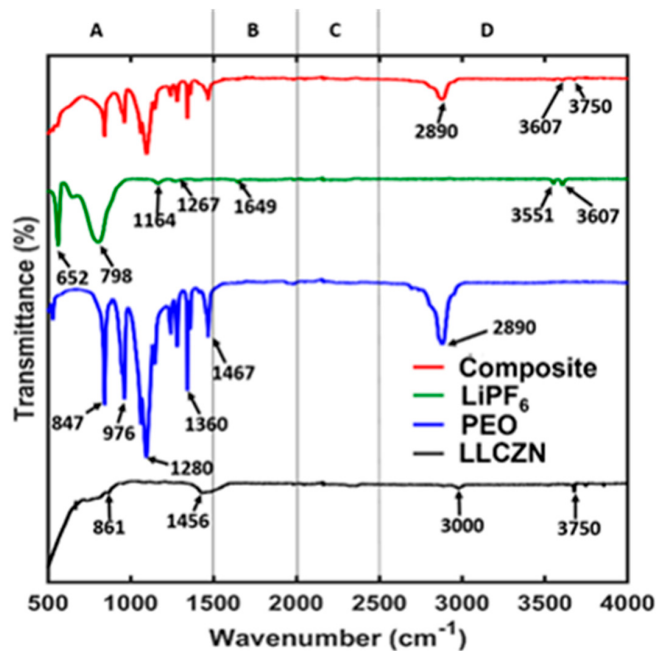

Figure 4. FTIR spectra of composite, LiPF$_6$, PEO, and LLCZN.

Figure 5 shows the thermogravimetric analysis of the LLCZN/PEO/LiPF$_6$ composite. As seen in Figure 5, the composite electrolyte exhibited a massive weight loss between 360 °C and 460 °C, which is a result of the decomposition of PEO and LiPF$_6$. The weight stabilized at 500 °C, and consisted mainly of the LLCZN garnet material because of its superior thermal stability. The remaining mass of 32.1% of LLCZN/PEO/LiPF$_6$ composite was the LLCZN in the composite, while pristine LLCZN (the insert) accounted for 99.1% at 600 °C. The loss of <1% of the remaining mass of the LLZCN can be attributed to experimental error. Additionally, LLCZN serves as a barrier between the anode and the cathode in case the polymer in the composite starts to melt at elevated temperatures [49].
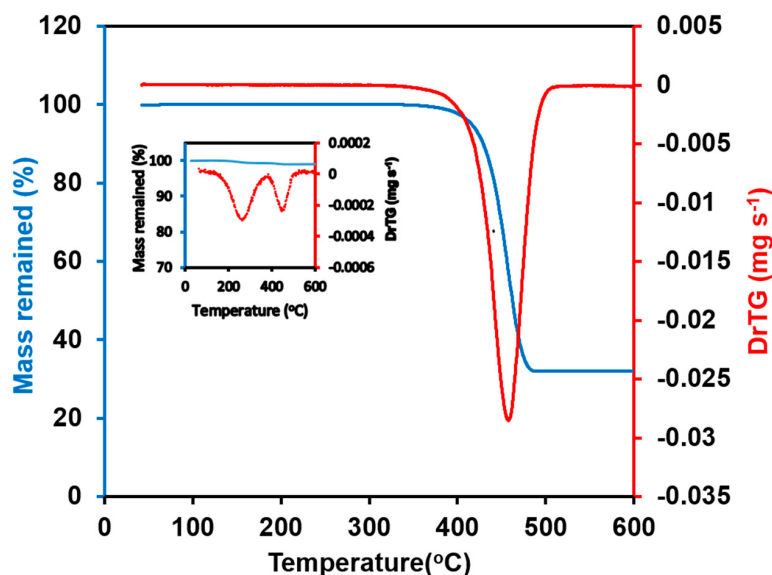

Figure 5. Thermogravimetric analysis (TGA) of LLCZN/PEO/LiPF$_6$ composite and the insert is pristine LLCZN powder.

Figure 6a shows the adsorption and desorption of N_2 on the $LLCZN/PEO/LiPF_6$ composite. It can be observed that as the pressure increased, the volume of N_2 adsorbed increased until the pores in the $LLCZN/PEO/LiPF_6$ composite became saturated, as indicated by the desorption curve. Increasing the relative pressure increases the volume of nitrogen adsorption. At a relative pressure of nearly 0.95, the pores were filled to the brim, holding a nitrogen volume of approximately 1.4 $cm^3\ g^{-1}$ of the sample. By releasing the pressure, the nitrogen began to desorb or evaporate. At a subsequent pressure of around 0.8, almost all the nitrogen was desorbed, giving rise to a narrow hysteresis, as shown by the desorption isotherm curve in Figure 6a. According to the international union of pure and applied chemistry (IUPAC) classification, this hysteresis is similar to type 1, which is associated with microporous materials consisting of well-defined cylindrical-type pore channels or agglomeration of compact uniform spheres [50]. It is also observed that the surface area and pore volume of the $LLCZN/PEO/LiPF_6$ composite were 0.114 $m^2\ g^{-1}$ and 7.92×10^{-4} $cm^{-3}\ g^{-1}$, respectively. The modal pore width was registered as being 402 Å, as depicted in Figure 6b, which shows that the $LLCZN/PEO/LiPF_6$ composite is nanoporous enough for lithium-ion movement during the charging and discharging process.
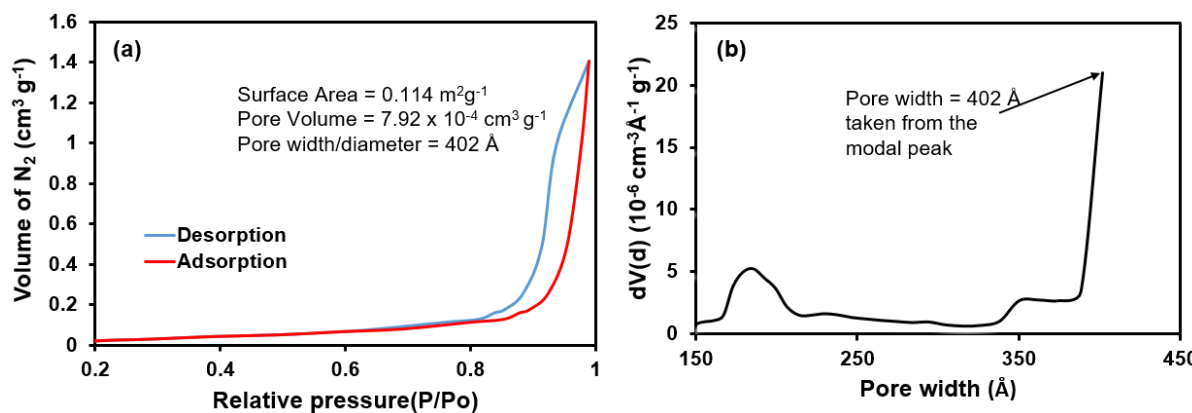

Figure 6. Brunauer–Emmett–Teller (BET) analysis of $LLCZN/PEO/LiPF_6$ composite: (**a**) adsorption–desorption isotherm curve and (**b**) pore size distribution.

The ionic conductivities calculated from the Nyquist plot (Figure 7) for the $LLCZN/PEO/LiPF_6$ composite with and without e-beam were 3.6×10^{-4} S cm^{-1} and 3.0×10^{-4} S cm^{-1}, respectively, and are in line with literature values for garnet materials. This is an indication that the ionic conductivity of our as-prepared $LLCZN/PEO/LiPF_6$ composite is almost the same as the $LLCZN/PEO/LiPF_6$ composite with e-beam.

Figure 8 represents the voltage–time profile of the first four cycles of a cell made with $LiCoO_2\,|\,LLCZN/PEO/LiPF_6\,|\,Li$ at different subsequent currents. It is observed that, as the current increased, the required time used for the charging and discharging decreased. At a current density of 0.05 mA cm^{-2}, it took approximately forty hours to charge and discharge each of the four cycles, Figure 8a. As we ramped up current density to 0.10 mA cm^{-2}, the charging and discharging time decreased to approximately seventeen hours, Figure 8b. As we further increased the current to 0.24 mA cm^{-2}, the charging and discharging time further decreased to approximately five hours, Figure 8c. The current of 0.50 mA cm^{-2}, which was close to the capacity of the battery analyzer, yielded a charging and discharging time of approximately one and half hours, Figure 8d. Finally, we ramped down the current and set to the original starting current of 0.05 mA cm^{-2} (final), and the charging and discharging time reduced slightly to 35 h, Figure 8e. This confirms that our device did not break down after subjecting it to different currents.
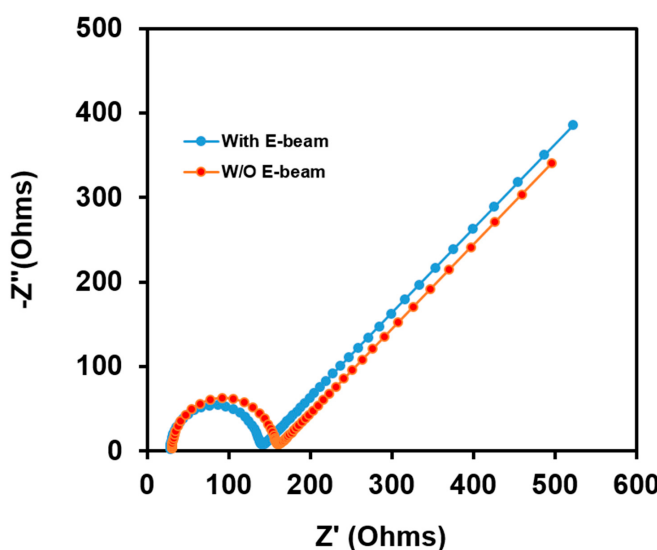
Figure 7. The electrochemical impedance spectra of LLCZN/PEO/LiPF$_6$ composite with and without e-beam.

Figure 8a–e show the discharge/charge curves for the first 20 cycles of the cell at different currents. At a current density of 0.05 mA cm^{-2}, the cell delivered a specific discharge capacity of 166 mAh g^{-1} during the 1st cycle, which gradually decreased to 162 mAh g^{-1} at the 4th cycle, Figure 8a, which is slightly higher than the practical capacity for LCO (140 mAh g^{-1}). This excess increase in practical capacity could be a result of the porous nature of the LLCZN/PEO/LiPF$_6$ solid-state electrolyte. Thereafter, we increased the current density to 0.10 mA cm^{-2} and recorded a specific discharge capacity of 150 mAh g^{-1} for the 1st cycle, which decreased to 145 mAh g^{-1} at the 4th cycle, as shown in Figure 8b. Figure 8c shows the specific discharge capacity of 104 mAh g^{-1} throughout the entire 4th cycling when a current density of 0.24 mA cm^{-2} was applied. Upon further cycling, we raised the current density to 0.50 mA cm^{-2} and the specific discharge capacity drastically decreased to 65 mAh g^{-1} for the whole four cycles, Figure 8d.

To monitor capacity recovery, we re-ran the test at the lower current density of 0.05 mA cm^{-2} (final). It was noticed that the specific discharge capacity ramped up to 152 mAh g^{-1} during the 1st cycle and gradually decreased to 150 mAh g^{-1} at the 4th cycle, as shown in Figure 8e. This is an indication that our device did not significantly break down during electrochemical testing under different currents. Interestingly, it was also observed that the specific discharge capacity was nearly the same for all four cycles under the applied current density values of 0.24 mA cm^{-2} and 0.50 mA cm^{-2}, Figure 8c,d. This can be attributed to the fact that the electrode/electrolyte interfaces were stable during cycling at these currents. Furthermore, the improved stability of PEO in the composite at high voltages of 3–4.5 V in our current study was caused by the surface modification of the SiO$_2$ coating layer via the e-beam technique. The coating layer reduced the oxidation of PEO at high voltage. The summarized cycle range, and the corresponding current and current densities used for the electrochemical testing, are listed in Table 1.

Table 1. Cycle range for different currents, current densities expressed in terms of area and mass.

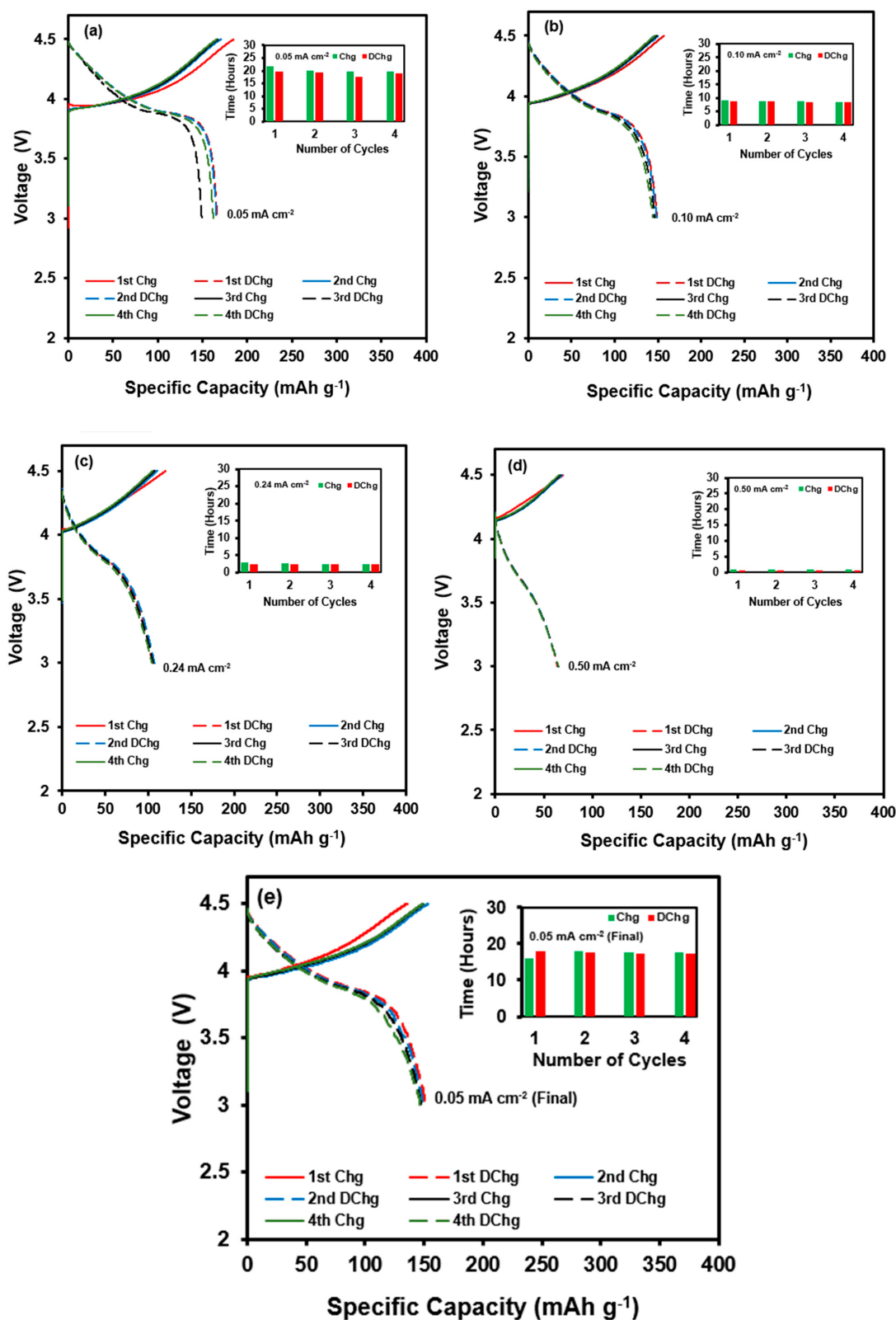| Cycle	Range Currents (mA)	Current Density (mA cm^{-2})	Current Density (mA g^{-1})
1–4	0.0945	0.05	8.50
5–8	0.189	0.10	17.0
9–12	0.475	0.24	43.0
13–16	0.945	0.50	85.0
17–20	0.0945	0.05	8.50

Figure 8. Charge–discharge voltage–time profiles and electrochemical performance of $LiCoO_2 | LLCZN/PEO/LiPF_6 | Li$ cells with voltage window of 3–4.5 V at different currents (**a**) 0.05 mA cm^{-2}, (**b**) 0.10 mA cm^{-2}, (**c**) 0.24 mA cm^{-2}, (**d**) 0.50 mA cm^{-2}, and (**e**) 0.05 mA cm^{-2} (final).

The cycling performance of a $LiCoO_2$ | LLCZN/PEO/LiPF$_6$ | Li cells in terms of specific capacity and specific energy, as well as their Coulombic and energy efficiencies, are depicted in Figure 9a,b, respectfully. The rate performance study for four cycles conducted at individual current densities of 0.05, 0.10, 0.24, 0.50 and 0.05 mA cm^{-2} at room temperature (22–25 °C), as shown in Figure 9a, yielded specific discharge capacities of 162, 152, 104, 65, and 152 mAh g^{-1} and Coulombic efficiencies of approximately 98% for all of the current densities not included in intercurrent transitions. Additionally, it was observed that the specific capacities increased with decreasing current densities, because lithium-ions diffusion occurs at lower densities. Similarly, specific discharge energy for the current densities above resulted in 663, 586, 393, 230 and 594 Wh kg^{-1} and energy efficiencies of approximately 90% for the entire 20 cycles, as shown in Figure 9b. The trends for both specific capacity and specific energy graphs follow the same sequence. Figure 9c shows the voltage–capacity curve of the coin cell for 130 cycles at a current density of 0.05 mA cm^{-2} (after subjecting it to 20 cycles at different currents as shown in Figure 9c,d, making it a total of 150 cycles). Again, as we increased the number of cycles, a minimal reduction in discharge capacity was observed, from 145 mAh g^{-1} to 130 mAh g^{-1}, in a voltage range of 3–4.5 V at room temperature (22–25 °C). This capacity is still high compared to what has been reported in the literature for a similar composite solid-state electrolyte (LLZTO/PEO/LiTFSi), which reached a specific capacity of 127 mAh g^{-1} after 50 cycles [10]. The cell retained 85% discharge capacity up to 150 cycles, with a Coulombic efficiency of 98% during the cycling process, Figure 9c.
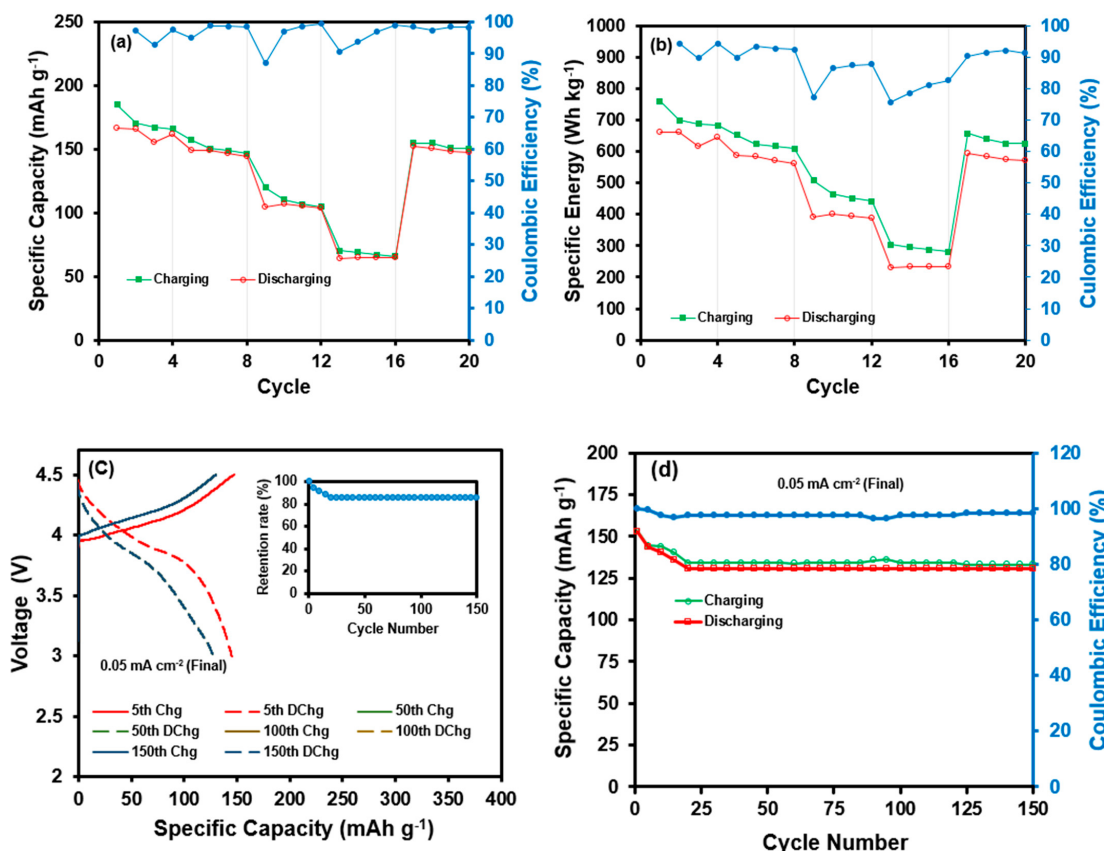

Figure 9. Electrochemical performance of $LiCoO_2$ | LLCZN/PEO/LiPF$_6$ | Li cells with voltage window of 3–4.5 V during the first 20 cycles at different currents: (**a**) specific capacity cycling performance; (**b**) specific energy cycling performance; (**c**) charge–discharge curve at 0.05 mA cm^{-2} for selected cycles; (**d**) cycling performance.

4. Conclusions

In summary, LLCZN/PEO/LiPF$_6$ solid-state electrolyte was synthesized using a facile sol–gel and pelletizing technique. The PEO matrix in the composite aids in bonding the composite solid-state electrolyte and electrodes to create a large contact area at the interface, thereby reducing the issue of large interfacial resistance and the battery continuously shows excellent electrochemical performance for many cycles. The LLCZN favors the movement of lithium-ions in the composite to enhance the lithium-ion conduction during charging and discharging cycles, whiles the LiPF$_6$ contributes more lithium ions into the composite via the transport path. The crystal structure and the identification of the chemical bond/species of the prepared composite solid electrolyte are confirmed through XRD and FTIR analysis which showed that the fabricated composite exhibit strong interaction between the pristine compounds. In addition, FESEM images at different magnifications revealed that the material is low density in nature and consists of highly interconnected porous structures with a size of 402 Å as confirmed by the BET data analysis. The prepared LLCZN/PEO/LiPF$_6$ solid-state electrolyte is used in a cell that has a strong electrochemical response and shows outstanding electrochemical stability, which remains at 130 mAh g^{-1} up to 50 charging and discharging cycles at 0.05 mA cm^{-2} current after subjecting the same coin cell to a high-current-rate performance test. Furthermore, the coin cell retains 85% discharge capacity up to 150 cycles with a Coulombic efficiency of approximately 98% and energy efficiency at 90% during the entire cycling process.

Author Contributions: Conceptualization, S.A.D.; methodology, S.A.D.; software, S.A.D.; validation, S.A.D.; J.S. and M.B.; formal analysis, S.A.D.; investigation, S.A.D.; resources, S.A.D.; data curation, S.A.D. and J.S.; writing—original draft preparation, S.A.D.; writing—review and editing, S.A.D.; J.S.; C.F.D.; S.K.P. and M.B.; visualization, S.A.D. and J.S.; supervision, M.B.; project administration, M.B.; funding acquisition, M.B. All authors have read and agreed to the published version of the manuscript.

Institutional Review Board Statement: Not applicable.

Informed Consent Statement: Not applicable.

Data Availability Statement: Not applicable.

Conflicts of Interest: The authors declare no conflict of interest.

References

1. Deng, J.; Bae, C.; Marcicki, J.; Masias, A.; Miller, T. Safety modelling and testing of lithium-ion batteries in electrified vehicles. *Nat. Energy* **2018**, *3*, 261–266. [CrossRef]
2. Srivastava, S.; Schaefer, J.L.; Yang, Z.; Tu, Z.; Archer, L.A. 25th Anniversary Article: Polymer-Particle Composites: Phase Stability and Applications in Electrochemical Energy Storage. *Adv. Mater.* **2013**, *26*, 201–234. [CrossRef]
3. Zhang, J.; Zhao, J.; Yue, L.; Wang, Q.; Chai, J.; Liu, Z.; Zhou, X.; Li, H.; Guo, Y.-G.; Cui, G.; et al. Safety-Reinforced Poly(Propylene Carbonate)-Based All-Solid-State Polymer Electrolyte for Ambient-Temperature Solid Polymer Lithium Batteries. *Adv. Energy Mater.* **2015**, *5*, 1501082. [CrossRef]
4. Zhang, J.; Zhao, N.; Zhang, M.; Li, Y.; Chu, P.; Guo, X.; Di, Z.; Wang, X.; Li, H. Flexible and ion-conducting membrane electrolytes for solid-state lithium batteries: Dispersion of garnet nanoparticles in insulating polyethylene oxide. *Nano Energy* **2016**, *28*, 447–454. [CrossRef]
5. Jiang, Y.; Yan, X.; Ma, Z.; Mei, P.; Xiao, W.; You, Q.; Zhang, Y. Development of the PEO Based Solid Polymer Electrolytes for All-Solid State Lithium Ion Batteries. *Polymers* **2018**, *10*, 1237. [CrossRef] [PubMed]
6. Fu, K.; Gong, Y.; Dai, J.; Gong, A.; Han, X.; Yao, Y.; Wang, C.; Wang, Y.; Chen, Y.; Yan, C.; et al. Flexible, solid-state, ion-conducting membrane with 3D garnet nanofiber networks for lithium batteries. *Proc. Natl. Acad. Sci. USA* **2016**, *113*, 7094–7099. [CrossRef] [PubMed]
7. Jiang, L.; Wang, Q.; Li, K.; Ping, P.; Jiang, L.; Sun, J. A self-cooling and flame-retardant electrolyte for safer lithium ion batteries. *Sustain. Energy Fuels* **2018**, *2*, 1323–1331. [CrossRef]

8. Kim, J.G.; Son, B.; Mukherjee, S.; Schuppert, N.; Bates, A.; Kwon, O.; Choi, M.J.; Chung, H.Y.; Park, S. A review of lithium and non-lithium based solid state batteries. *J. Power Source* **2015**, *282*, 299–322. [CrossRef]

9. Yoon, Y.; Park, C.; Kim, J.; Shin, D. Lattice orientation control of lithium cobalt oxide cathode film for all-solid-state thin film batteries. *J. Power Source* **2012**, *226*, 186–190. [CrossRef]

10. Li, Y.; Zhou, W.; Xin, S.; Li, S.; Zhu, J.; Lü, X.; Cui, Z.; Jia, Q.; Zhou, J.; Zhao, Y.; et al. Fluorine-Doped Antiperovskite Electrolyte for All-Solid-State Lithium-Ion Batteries. *Angew. Chem. Int. Ed.* **2016**, *55*, 9965–9968. [CrossRef]

11. Manthiram, A.; Yu, X.; Wang, S. Lithium battery chemistries enabled by solid-state electrolytes. *Nat. Rev. Mater.* **2017**, *2*, 16103. [CrossRef]

12. Nan, C.-W.; Fan, L.-Z.; Lin, Y.; Cai, Q. Enhanced Ionic Conductivity of Polymer Electrolytes Containing Nanocomposite-SiO2Particles. *Phys. Rev. Lett.* **2003**, *91*, 266104. [CrossRef]

13. Zhao, W.; Yi, J.; He, P.; Zhou, H. Solid-State Electrolytes for Lithium-Ion Batteries: Fundamentals, Challenges and Perspectives. *Electrochem. Energy Rev.* **2019**, *2*, 574–605. [CrossRef]

14. Chen, L.; Li, Y.; Li, S.-P.; Fan, L.-Z.; Nan, C.-W.; Goodenough, J.B. PEO/garnet composite electrolytes for solid-state lithium batteries: From "ceramic-in-polymer" to "polymer-in-ceramic". *Nano Energy* **2018**, *46*, 176–184. [CrossRef]

15. Long, L.; Wang, S.; Xiao, M.; Meng, Y. Polymer electrolytes for lithium polymer batteries. *J. Mater. Chem. A* **2016**, *4*, 10038–10069. [CrossRef]

16. Armand, M. Polymer solid electrolytes—An overview. *Solid State Ion.* **1983**, *9–10*, 745–754. [CrossRef]

17. Zhou, W.; Wang, S.; Li, Y.; Xin, S.; Manthiram, A.; Goodenough, J.B. Plating a Dendrite-Free Lithium Anode with a Polymer/Ceramic/Polymer Sandwich Electrolyte. *J. Am. Chem. Soc.* **2016**, *138*, 9385–9388. [CrossRef]

18. Cao, C.; Li, Z.-B.; Wang, X.-L.; Zhao, X.-B.; Han, W.-Q. Recent Advances in Inorganic Solid Electrolytes for Lithium Batteries. *Front. Energy Res.* **2014**, *2*, 25. [CrossRef]

19. Li, Y.; Wang, C.-A.; Xie, H.; Cheng, J.; Goodenough, J.B. High lithium ion conduction in garnet-type $Li_6La_3ZrTaO_{12}$. *Electrochem. Commun.* **2011**, *13*, 1289–1292. [CrossRef]

20. Homann, G.; Stolz, L.; Nair, J.; Laskovic, I.C.; Winter, M.; Kasnatscheew, J. Poly(Ethylene Oxide)-based Electrolyte for Solid-State-Lithium-Batteries with High Voltage Positive Electrodes: Evaluating the Role of Electrolyte Oxidation in Rapid Cell Failure. *Sci. Rep.* **2020**, *10*, 4390. [CrossRef] [PubMed]

21. Liu, Z.; Li, H.; Zhu, M.; Huang, Y.; Tang, Z.; Pei, Z.; Wang, Z.; Shi, Z.; Liu, J.; Zhi, C. Towards wearable electronic devices: A quasi-solid-state aqueous lithium-ion battery with outstanding stability, flexibility, safety and breathability. *Nano Energy* **2018**, *44*, 164–173. [CrossRef]

22. Chen, Y.-M.; Hsu, S.-T.; Tseng, Y.-H.; Yeh, T.-F.; Hou, S.-S.; Jan, J.-S.; Lee, Y.-L.; Teng, H. Minimization of Ion-Solvent Clusters in Gel Electrolytes Containing Graphene Oxide Quantum Dots for Lithium-Ion Batteries. *Small* **2018**, *14*, e1703571. [CrossRef]

23. Xu, H.; Wang, S.; Wilson, H.; Zhao, F.; Manthiram, A. Y-Doped NASICON-type $LiZr_2$ $(PO_4)_3$ Solid Electrolyte for Lithium–Metal Batteries. *Chem. Mater.* **2017**, *29*, 7206–7212. [CrossRef]

24. Sun, C.; Liu, J.; Gong, Y.; Wilkinson, D.P.; Zhang, J. Recent advances in all-solid-state rechargeable lithium batteries. *Nano Energy* **2017**, *33*, 363–386. [CrossRef]

25. Wang, L.; Li, X.; Yang, W. Enhancement of electrochemical properties of hot-pressed poly(ethylene oxide)-based nanocomposite polymer electrolyte films for all-solid-state lithium polymer batteries. *Electrochim. Acta* **2010**, *55*, 1895–1899. [CrossRef]

26. Thangadurai, V.; Kaack, H.; Weppner, W.J.F. Novel Fast Lithium Ion Conduction in Garnet-Type $Li_5La_3M_2O_{12}$ (M = Nb, Ta). *J. Am. Ceram. Soc.* **2003**, *86*, 437–440. [CrossRef]

27. Murugan, R.; Thangadurai, V.; Weppner, W. Fast Lithium Ion Conduction in Garnet-Type $Li_7La_3Zr_2O_{12}$. *Angew. Chem. Int. Ed.* **2007**, *46*, 7778–7781. [CrossRef] [PubMed]

28. Bruce, P.G. Solid-state chemistry of lithium power sources. *Chem. Commun.* **1997**, 1817–1824. [CrossRef]

29. Croce, F.; Appetecchi, G.B.; Persi, L.; Scrosati, B. Nanocomposite polymer electrolytes for lithium batteries. *Nature* **1998**, *394*, 456–458. [CrossRef]

30. Croce, F.; Persi, L.; Ronci, F.; Scrosati, B. Nanocomposite polymer electrolytes and their impact on the lithium battery technology. *Solid State Ion.* **2000**, *135*, 47–52. [CrossRef]

31. Xi, J.; Tang, X. Nanocomposite polymer electrolyte based on Poly(ethylene oxide) and solid super acid for lithium polymer battery. *Chem. Phys. Lett.* **2004**, *393*, 271–276. [CrossRef]

32. Lightfoot, P.; Mehta, M.A.; Bruce, P.G. Crystal Structure of the Polymer Electrolyte Poly(ethylene oxide) 3: $LiCF_3SO_3$. *Science* **1993**, *262*, 883–885. [CrossRef] [PubMed]

33. Quartarone, E.; Mustarelli, P. Electrolytes for solid-state lithium rechargeable batteries: Recent advances and perspectives. *Chem. Soc. Rev.* **2011**, *40*, 2525–2540. [CrossRef] [PubMed]

34. Christie, A.M.; Lilley, S.J.; Staunton, E.; Andreev, Y.G.; Bruce, P.G. Increasing the conductivity of crystalline polymer electrolytes. *Nature* **2005**, *433*, 50–53. [CrossRef] [PubMed]

35. Appetecchi, G.; Croce, F.; Persi, L.; Ronci, F.; Scrosati, B. Transport and interfacial properties of composite polymer electrolytes. *Electrochim. Acta* **2000**, *45*, 1481–1490. [CrossRef]

36. Magistris, A. Transport and thermal properties of (PEO)n–$LiPF_6$ electrolytes for super-ambient applications. *Solid State Ion.* **2000**, *136–137*, 1241–1247. [CrossRef]

37. Zhao, C.-Z.; Zhang, X.-Q.; Cheng, X.-B.; Zhang, R.; Xu, R.; Chen, P.-Y.; Peng, H.-J.; Huang, J.-Q.; Zhang, Q. An anion-immobilized composite electrolyte for dendrite-free lithium metal anodes. *Proc. Natl. Acad. Sci. USA* **2017**, *114*, 11069–11074. [CrossRef]

38. Liu, W.; Liu, N.; Sun, J.; Hsu, P.-C.; Li, Y.; Lee, H.-W.; Cui, Y. Ionic Conductivity Enhancement of Polymer Electrolytes with Ceramic Nanowire Fillers. *Nano Lett.* **2015**, *15*, 2740–2745. [CrossRef] [PubMed]

39. Han, X.; Gong, Y.; Fu, K.; He, X.; Hitz, G.T.; Dai, J.; Pearse, A.; Liu, B.; Wang, H.; Rubloff, G.; et al. Negating interfacial impedance in garnet-based solid-state Li metal batteries. *Nat. Mater.* **2016**, *16*, 572–579. [CrossRef]

40. Liu, W.; Lee, S.W.; Lin, D.; Shi, F.; Wang, S.; Sendek, A.D.; Cui, Y. Enhancing ionic conductivity in composite polymer electrolytes with well-aligned ceramic nanowires. *Nat. Energy* **2017**, *2*, 17035. [CrossRef]

41. Danquah, S. Performance of hybrid $SnO_2/Li_2FeMn_3O_8$ nanostructured electrode for efficient Li ion storage application. *Atlas J. Mater. Sci.* **2020**, 90–98. [CrossRef]

42. Qian, X.; Gu, N.; Cheng, Z.; Yang, X.; Wang, E.; Dong, S. Methods to study the ionic conductivity of polymeric electrolytes using a.c. impedance spectroscopy. *J. Solid State Electrochem.* **2001**, *6*, 8–15. [CrossRef]

43. Liu, J.-W.; Li, X.-H.; Wang, Z.-X.; Guo, H.-J.; Peng, W.-J.; Zhang, Y.-H.; Hu, Q.-Y. Preparation and characterization of lithium hexafluorophosphate for lithium-ion battery electrolyte. *Trans. Nonferrous Met. Soc. China* **2010**, *20*, 344–348. [CrossRef]

44. Ahmed, H.T.; Abdullah, O.G. Preparation and Composition Optimization of PEO:MC Polymer Blend Films to Enhance Electrical Conductivity. *Polymers* **2019**, *11*, 853. [CrossRef] [PubMed]

45. Bhide, A.; Hariharan, K. Ionic transport studies on (PEO)6:NaPO3 polymer electrolyte plasticized with PEG400. *Eur. Polym. J.* **2007**, *43*, 4253–4270. [CrossRef]

46. Nandiyanto, A.B.D.; Oktiani, R.; Ragadhita, R. How to Read and Interpret FTIR Spectroscope of Organic Material. *Indones. J. Sci. Technol.* **2019**, *4*, 97–118. [CrossRef]

47. Kalaiselvimary, J.; Prabhu, M.R. Fabrications and investigation of physicochemical and electrochemical properties of heteropoly acid-doped sulfonated chitosan-based polymer electrolyte membranes for fuel cell applications. *Polym. Bull.* **2018**, *76*, 1401–1422. [CrossRef]

48. Shahitha, P.J.; Abdul Majeed, S.S.M. Poly (ethylene oxide)/Polyurethane based gel polymer electrolytes for lithium batteries. *Int. J. Sci. Eng. Res.* **2013**, *4*, 553–558.

49. Zhou, D.; He, Y.-B.; Liu, R.; Liu, M.; Du, H.; Li, B.; Cai, Q.; Yang, Q.-H.; Kang, F. In Situ Synthesis of a Hierarchical All-Solid-State Electrolyte Based on Nitrile Materials for High-Performance Lithium-Ion Batteries. *Adv. Energy Mater.* **2015**, *5*, 1500353. [CrossRef]

50. Sing, K.S.W.; Everett, D.H.; Haul, R.A.W.; Moscou, L.; Pierotti, R.A.; Rouquerol, J. Reporting physisorption data for gas/solid systems with special reference to the determination of surface area and porosity (Recommendations 1984). *Pure Appl. Chem.* **1985**, *57*, 603609. [CrossRef]